

# Multiple Targets Localization Behind L-Shaped Corner via UWB Radar

Songlin Li , Shisheng Guo , *Member, IEEE*, Jiahui Chen , Xiaqing Yang , *Student Member, IEEE*, Shihao Fan, Chao Jia, Guolong Cui , *Senior Member, IEEE*, and Haining Yang , *Member, IEEE*

**Abstract**—This paper deals with the multiple targets localization problem via multi-channel ultra-wideband (UWB) imaging radar non-line-of-sight (NLOS) signal processing. A novel matching-based radar imaging algorithm is proposed to obtain the positions of multiple targets in the L-shaped corner scenario with complex multipath ghost signals. Firstly, a multipath propagation model for the multiple targets scenario is established. Then the positions of the actual multipath ghosts are extracted from the radar image, and the candidate targets corresponding to these multipath ghosts are derived. Secondly, the ellipse-cross-localization method is proposed to obtain the positions of the candidate multipath ghosts, followed by two defined matching factors to measure the similarity between actual and candidate multipath ghosts. According to the similarity, decision rules are designed to determine the actual targets. Compared with the localization algorithm based on one-dimensional range profile, the proposed algorithm can effectively cope with the cases of multiple targets, even in the cases of rough walls and noise. Finally, simulations and experimental data are used to validate the effectiveness of the proposed algorithm.

**Index Terms**—Multi-channel UWB radar, multipath exploitation, multiple targets localization, NLOS L-shaped corner.

## I. INTRODUCTION

**R**ADAR surveillance technology in urban environment is important in various applications, such as urban battles, antiterrorism actions, and disaster rescues, etc [1]–[3]. Recently, radar system has emerged as one of the key technologies in autonomous driving systems, providing environmental perception in all weather conditions [4]–[7]. In general, the autonomous driving systems should not only properly react to a threat, but also predict imminent, dangerous, driving situation. For instance, a vehicle-A can detect approaching vehicle-B in advance in non-line-of-sight (NLOS) conditions, especially at

urban crossroads. Unlike the conventional sensor applications where vehicles are in the line-of-sight (LOS) area of the sensor systems, in these cases, the vehicle is always located in a shadow area surrounded by multiple buildings. To detect the vehicles, the multipath derived from diffraction and reflection on building surfaces are exploited in many recently works [8]–[12].

Some preliminary works have been done to demonstrate the feasibility of detection of the NLOS targets using the multipath radar returns. Theoretical works aiming at establishing the ray-tracing propagation model was done in [13]. Meanwhile, the authors also analyzed the degradation of power and coherency in signal processing due to wall surface roughness. Several experiments were conducted in [14]–[16] to prove the feasibility of corner targets detection. In [14], the Range-Doppler (RD) images were generated to show the discrimination of moving targets by using multipath returns in LOS and NLOS situations. In [15] and [16], the multipath was also utilized to obtain the micro-doppler features from moving targets.

In some other works, several techniques have been developed to obtain the two-dimensional positions of NLOS targets. In [17], the authors first proposed a detection method of NLOS targets in a realistic scene. As a continuation of this work, they proposed moving NLOS targets positioning algorithm based on numerical simulations in [18]. Specifically, a scanning, narrow beam radar system was utilized to prevent mutual interference of various multipath. Combining the knowledge of radar beam direction and the detection distance of the targets, the position of targets could be obtained easily. However, this solution assumed that the radar can provide enough angular resolution to cover all monitored surfaces which is not always available.

Different from the narrow beam radar system, the angle information for different multipaths can not be obtained by the wide beam radar system, leading to the ambiguities of the target different multipaths. To tackle this problem, there are some algorithms have been proposed. For instance, in [19], the authors proposed a target localization method based on diffraction path, one-bounce reflection path and their combinations. Experimental results showed that the target was well-positioned depending on the proposed algorithm. However, two or more-bounce reflection paths were not taken into account in their method, which may not be suitable in other situations. In [20], the authors first provided an ideal signal model under the assumption that the signals propagating by all multipaths can be received, then the particle filter method was exploited to track a single NLOS target. Simulation results validated the efficiency of the algorithm. In [21], the

Manuscript received March 31, 2020; revised September 30, 2020 and January 9, 2021; accepted March 14, 2021. Date of publication March 23, 2021; date of current version May 5, 2021. This work was supported in part by the National Natural Science Foundation of China under Grants 62001091, 61871080, 61701088, and 61701093, in part by the Initial Scientific Research Foundation of UESTC under Grant Y030202059018051, in part by ChangJiang Scholar Program, in part by the GF Science, and Technology Special Innovation Zone Project. The review of this article was coordinated by Dr. Balasubramaniam Natarajan. (Corresponding author: Shisheng Guo.)

The authors are with the School of Information and Communication Engineering, University of Electronic Science and Technology of China, Chengdu 611731, China (e-mail: lsl@std.uestc.edu.cn; ssguo@uestc.edu.cn; jiahuichen@std.uestc.edu.cn; yxqvalerie0711@hotmail.com; 765992517@qq.com; jiachao@uestc.edu.cn; cuiguolong@uestc.edu.cn; hnyang@uestc.edu.cn).

Digital Object Identifier 10.1109/TVT.2021.3068266

TABLE I  
COMPARISON OF EM SIMULATION RESULTS IN FOUR CASES

Case	Number of targets	SNR(dB)	Smooth/Rough	MLE(cm)
Case-1	1	20	Smooth	0.09
Case-2	1	10	Smooth	0.13
Case-3	2	20	Smooth	0.16
Case-4	2	20	Rough	0.25

TABLE II  
KEY PARAMETERS OF MULTI-CHANNEL UWB RADAR SYSTEM

Parameters	Value
Starting frequency	1.5 GHz
Ending frequency	2.1 GHz
Bandwidth	600 MHz
Number of steps	301
Frequency step	2 MHz
Radiation power	18 dBm

matched filter algorithm and the square law combiner algorithm were utilized to handle the information provided by multipath returns to detect and estimate the position of the NLOS target.

Furthermore, our previous experimental works were also carried out to test the feasibility of locating a single target in the absence of LOS with real measurements [22]–[25]. Note that these techniques aforementioned can not completely solve the localization problem of the multiple targets in the NLOS environment. In addition to the mutual interference between targets, the ambiguities between different multipaths of the targets are the biggest challenge for multiple targets localization in the NLOS environment. It is difficult to detect and locate multiple targets only by range profile.

Different from the above mentioned single target localization techniques, we consider a multiple targets localization problem via NLOS signals in an L-shaped corner environment based on multi-channel ultra-wideband (UWB) imaging radar, of which the preliminary research results have been reported in [26]. In this paper, the deep analysis and results are presented. First, we establish a multipath propagation model in the multiple targets scenario for time division multiple-input-multiple-output (MIMO) radar and analyze the characters of the measured signals and radar images containing multipath ghosts. Then, a novel multiple targets localization algorithm based on multipath ghost image matching is proposed. Compared with the localization algorithm based on a one-dimensional range profile, the proposed approach can achieve good multiple targets positioning performance, even in the cases of rough walls and noise.

The rest of the paper is organized as follows. In Section II, we first establish the signal propagation model in an L-shaped corner scenario and then analyse the characters of the measured signals and radar images containing multipath ghosts. In Section III, multiple targets localization algorithm based on image matching is proposed. In Section IV, numerical simulation and experiments data validate the proposed algorithm. Section V concludes this paper.

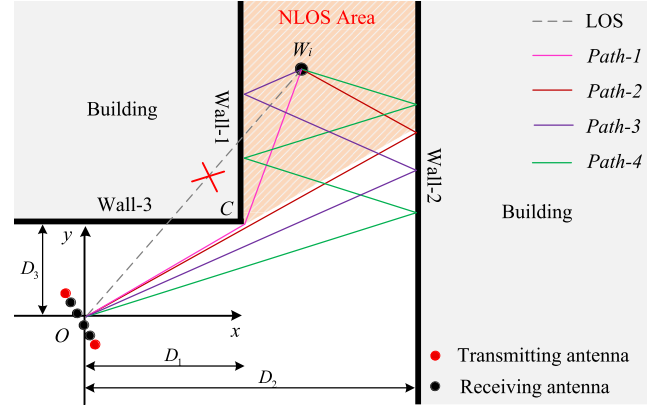


Fig. 1. Multipath propagation model in the L-shaped corner scenario.

## II. PROBLEM FORMULATION

### A. Signal Model

Consider a scenario containing an L-shaped corner with three walls, named Wall-1, Wall-2 and Wall-3, as shown in Fig. 1.  $\mathbf{C} = [x_c, y_c]^T$  is a corner formed by Wall-1 and Wall-3. The location and extent  $D_i, i = 1, 2, 3$  of the Wall-1, Wall-2 and Wall-3 are assumed known. A total of  $N_w$  targets  $\mathbf{W}_i = [x_{wi}, y_{wi}]^T, i = 1, 2, \dots, N_w$  are located at one side of the corner, that is in the corridor of Wall-1 and Wall-2. To detect these hidden targets, a multi-channel UWB radar [27] with  $M$  transmitting antennas and  $N$  receiving antennas is placed at another side of the corner. The array center is located at coordinate origin  $\mathbf{O} = [x_o, y_o]^T$ . Thus, it is situated in a way that it is invisible for a moving target which is behind the corner.

We assume that the layout of the L-shaped corner scenario and the position of the radar are known *a priori* in this paper. It is supposed that the  $m$ th transmitting antenna located at  $\mathbf{T}_m = [x_{tm}, y_{tm}]^T$  transmits signal  $s(t)$ . The echoes received by the  $n$ th receiving antenna located at  $\mathbf{R}_n = [x_{rn}, y_{rn}]^T$ , is expressed as

$$s_{r,mn}(t) = \sum_{p,q} \sigma_{i,p}^{(m)} \sigma_{i,q}^{(n)} s\left(t - \tau_{i,p}^{(m)} - \tau_{i,q}^{(n)}\right) + \xi(t) + \eta(t), i = 1, 2, \dots, N_w, \quad (1)$$

where  $\tau_{i,p}^{(m)}$  represents the time delay of transmitting path and  $\sigma_{i,p}^{(m)}$  is the transmitting attenuation coefficient, while  $\tau_{i,q}^{(n)}$  denotes the time delay of the receiving path and  $\sigma_{i,q}^{(n)}$  is the receiving attenuation coefficient,  $p$  and  $q$  are the number of transmitting paths and receiving paths which the ray travel to the target or radar via diffraction or reflection path, respectively,

$\xi(t)$  is the received direct-coupled signal by the receiver from the transmitter and summarizes the clutters caused by strong reflections from walls,  $\eta(t)$  denotes the noise in the environment.

### B. Multipath Propagation Model

In the L-shaped corner environment, the multipaths derived from diffraction and multi-bounce on building corners or surfaces can be utilized to detect the hidden targets. Note that the signals propagating to the target via four or more-bounce propagating paths attenuate seriously, only four types of single-trip propagating paths named *Path-1*, *Path-2*, *Path-3* and *Path-4* are considered in this paper, namely,  $p \in \{1, 2, 3, 4\}$  and  $q \in \{1, 2, 3, 4\}$  (see Fig. 1). In addition, real-data experiments have shown that more-bounce reflections suffer from severe attenuation and may be too weak to be observed. The same conclusion was also observed in our previous works [23].

Wherein *Path-1*, the signals propagate to the target by diffraction on corner  $C$ . In *Path-2*, *Path-3* and *Path-4*, the signals propagate to the target by one-bounce, two-bounce and three-bounce reflection between Wall-1 and Wall-2, respectively. Since both the transmitted and received signals may pass through these four single-trip propagating paths, there will be sixteen different round-trip paths. For convenience, stacking all these paths  $a_{pq}$  in a matrix  $\Psi$ , we have

$$\Psi = \begin{bmatrix} a_{11} & a_{12} & \cdots & a_{1q} \\ a_{21} & a_{22} & \cdots & a_{2q} \\ \vdots & \vdots & \ddots & \vdots \\ a_{p1} & a_{p2} & \cdots & a_{pq} \end{bmatrix}, \quad (2)$$

where  $a_{pq}$  denotes the round-trip paths combined with the  $p$ th transmitting path and the  $q$ th receiving path  $\{p = 1, 2, 3, 4, q = 1, 2, 3, 4\}$ .

The real aperture of multi-channel radar must be small enough to prevent the radar from being exposed to threat target in the corner environment. Therefore, the distance of each transmitter and receiver is usually small. For each pair of transmitter and receiver, the length difference between the round-trip path  $a_{pq}, p \neq q$  and  $a_{qp}, p \neq q$  is too small to be distinguished, that is

$$\left\{ \begin{array}{l} l_{a_{12}} \approx l_{a_{21}}, l_{a_{13}} \approx l_{a_{31}}, l_{a_{14}} \approx l_{a_{41}} \\ l_{a_{23}} \approx l_{a_{32}}, l_{a_{24}} \approx l_{a_{42}}, l_{a_{34}} \approx l_{a_{43}} \end{array} \right\}, \quad (3)$$

where  $l_{a_{pq}}$  denotes the path length of  $a_{pq}$ . Moreover, the size and expansion of the target to be detected need to be considered.

Without loss of generality, we assume that the target  $W_i, i = 1, 2, \dots, N_w$  has existed in the L-shaped corner scenario. For diffraction path  $a_{1p}$  or  $a_{q1}, p = 1, 2, 3, 4, q = 1, 2, 3, 4$ , according to the uniform geometrical theory of diffraction (UTD) [28], an equivalent virtual target  $W'_{i,1}$  related to diffraction is obtained, which is located on the circle with centered at corner  $C$ , as shown in Fig. 2.

$$\mathbf{W}_{i,1} = [x_1, y_1]^T \in \left\{ (x - x_c)^2 + (y - y_c)^2 = l_w^2 \right\}, \quad (4)$$

where  $l_w$  denotes the distance from the corner  $C$  to  $W_i$ .

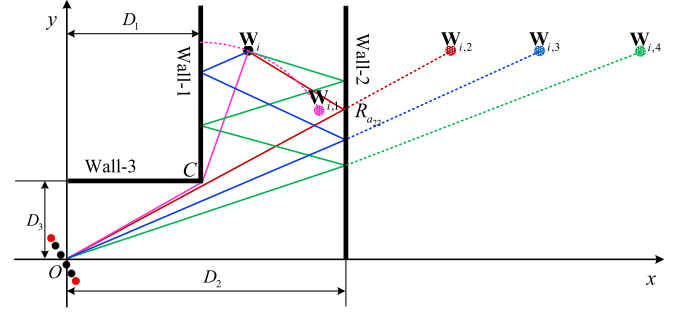


Fig. 2. Equivalent virtual targets related to the diffraction and reflection.

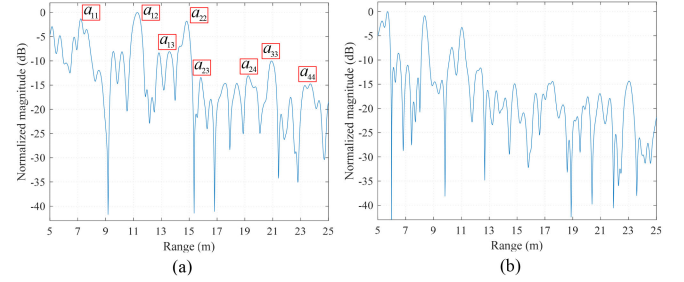


Fig. 3. Single channel echo of experimental results. (a) Echo of the single target. (b) Echo of the multiple targets.

Furthermore, each of the reflection propagation path will give rise to equivalent virtual target, denoted as  $\mathbf{W}_{i,p}, p = 2, 3, 4$ , which can be calculated as

$$\begin{cases} \mathbf{W}_{i,2} = [x_2, y_2]^T = [2D_2 - x_w, y_w]^T, \\ \mathbf{W}_{i,3} = [x_3, y_3]^T = [2D_2 - 2D_1 + x_w, y_w]^T, \\ \mathbf{W}_{i,4} = [x_4, y_4]^T = [4D_2 - 2D_1 - x_w, y_w]^T. \end{cases} \quad (5)$$

According to the propagation characteristics of diffraction and reflection, the delay time of the transmit path  $\tau_{i,p}^{(m)}$  in Eq. (1) can be obtained as

$$\tau_{i,p}^{(m)} = \begin{cases} \frac{\|\mathbf{T}_m \mathbf{C}\|}{c} + \frac{\|\mathbf{W}_{i,p} \mathbf{C}\|}{c}, p = 1, \\ \frac{\|\mathbf{T}_m \mathbf{W}_{i,p}\|}{c}, p = 2, 3, 4, \end{cases} \quad (6)$$

where  $\|\cdot\|$  represents Euclidean distance,  $c$  denotes the propagation velocity of electromagnetic (EM) waves. Similarly, the delay time of the receive path  $\tau_{i,q}^{(n)}$  in Eq. (1) can be calculated as

$$\tau_{i,q}^{(n)} = \begin{cases} \frac{\|\mathbf{R}_n \mathbf{C}\|}{c} + \frac{\|\mathbf{W}_{i,q} \mathbf{C}\|}{c}, q = 1, \\ \frac{\|\mathbf{R}_n \mathbf{W}_{i,q}\|}{c}, q = 2, 3, 4. \end{cases} \quad (7)$$

### C. Target and Multipath Images

To analyse the characters of the measured signals, single channel echoes of the single target and multiple targets measured by UWB radar in the L-shaped corner scenario are shown respectively in Fig. 3. Note that the carrier frequency and the bandwidth of the signal are 1 GHz and 0.815 GHz, respectively.

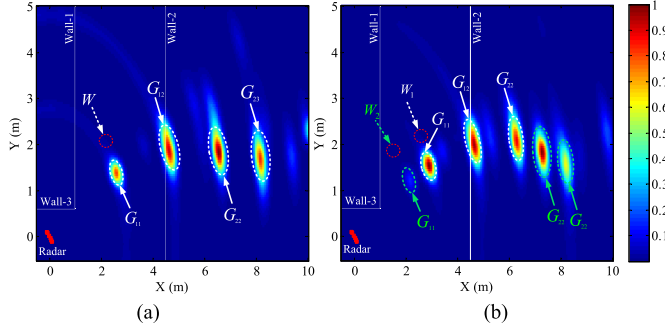


Fig. 4. BP imaging results in the L-shaped corner scenario. (a) Imaging result of the single target. (b) Imaging result of the multiple targets.

The strong reflection echoes produced by surrounding buildings and the direct-coupled signals in Eq. (1) have been removed by using moving target indicator (MTI) filtering method [29]. Based on the known layout of the scenario and position of the target, the length of all round-trip paths in  $\Psi$  can be calculated.

Fig. 3 (a) shows that most of the multipath propagation paths aforementioned appear. Except for the round-trip path combined with the diffraction transmitting/receiving path and the fourth transmitting/receiving path, these peaks of the round-trip paths are clear enough to be extracted. However, in the case of multiple targets, since the returns are overlapped and the interference between different targets have existed, we can not pick out types of the specific path for different targets from the range profile, as shown in Fig. 3 (b). Therefore, it is difficult to detect and locate the hidden multiple targets based on the one-dimensional range profile.

Accordingly, the two-dimensional radar images including targets and multipath ghosts are creatively utilized to determine the location of the targets in this paper. Based on radar returns, the back-projection (BP) imaging algorithm is utilized to form a radar image [30]. Specifically, the imaging region is equally divided into  $X \times Y$  pixels, where the coordinates of pixel  $\chi$  can be denoted by

$$\mathbf{Z}_\chi = (x_{Ro}, y_{Co}), Ro = 1, 2, \dots, X, Co = 1, 2, \dots, Y. \quad (8)$$

where  $Ro$  and  $Co$  are represent pixels on the  $x$ -axis and  $y$ -axis, respectively. Then, the value of image pixel  $\chi$  can be calculated as

$$\mathbf{I}_{BP}(\mathbf{Z}_\chi) = \sum_{m=1}^M \sum_{n=1}^N s_{r,mn} \left( \tau_{i,p}^{(m)}(x, y) + \tau_{i,q}^{(n)}(x, y) \right), \quad (9)$$

where  $\tau_{i,p}^{(m)}(x, y)$  and  $\tau_{i,q}^{(n)}(x, y)$  are the time delay of transmitting path and receiving path at pixel  $(x, y)$ , respectively.

Repeat the process until all the pixels of the region are calculated to form the whole image. Fig. 4 (a) shows that imaging result with single target, where  $G_{pq}$  denotes the multipath ghost derived from the round-trip path  $a_{pq}$ ,  $W$  is actual target position. Meanwhile, the radar image of multiple targets is shown in Fig. 4 (b), in which the actual position and ghost position of the target  $W_1$  and  $W_2$  are marked with different colors, respectively.

As shown the one-dimensional range profile of multiple targets in Fig. 3(b), it is difficult to determine the corresponding peaks of different targets, which makes it impossible to obtain targets position by the previous method [18], [23]. It can be seen that there are many multipath ghosts with respect to the round-trip paths aforementioned in Fig. 4, in which the target does not appear in the actual position in the image because of the loss of the LOS return.

Benefit from multi-channel radar virtual array synthesis technology, it is possible to extract the multipath ghosts of different targets. Meanwhile, the positions of these multipath ghosts are closely related to the targets' location. On the basis of the analysis above, we propose a novel multiple targets localization method by matching these multipath ghosts based on the two-dimensional radar image in next section.

### III. MULTIPLE TARGETS LOCALIZATION METHOD BASED ON MULTIPATH GHOSTS IMAGES MATCHING

In this section, we introduce the targets localization method by exploiting multipath ghosts in radar image, that is multiple targets localization method based on multipath ghosts images matching. We elaborate details process in the following subsections.

#### A. Multipath Ghost Position Extraction

In this subsection, we extract the positions of the ghosts caused by the multipaths aforementioned. After that, the position distribution characteristics of the one bounce ghosts are analyzed.

First, in order to extract the positions of the multipath ghosts, we obtain a binary image  $\mathbf{I}_b(\cdot)$  after threshold detection, expressed as

$$\mathbf{I}_b(\mathbf{Z}_\chi) = \begin{cases} 1, & \mathbf{I}_{BP}(\mathbf{Z}_\chi) \geq T_a, \\ 0, & \mathbf{I}_{BP}(\mathbf{Z}_\chi) < T_a, \end{cases} \quad (10)$$

where  $T_a$  is a threshold of binary detection, which is proportional to the maximum value of  $\mathbf{I}_{BP}(\mathbf{Z}_\chi)$ , computed by

$$T_a = \alpha \max(\mathbf{I}_{BP}(\mathbf{Z}_\chi)), \quad (11)$$

where  $\alpha$  is an empirical parameter, which is used to control the probability of filtering clutter and preserving the focus regions.

Then, the bwlable function in Matlab is adopted [31], [32], which returns the label matrix that contains labels for the 8-connected objects found in 2-D binary images. The connected domains can be extracted from the binary image above. Finally, the centroid of each connected domain is calculated as the position of the multipath ghost, denoted by  $\mathbf{G}_l = [x_l, y_l]^T$ , i.e.

$$\begin{cases} x_l = \frac{1}{N_l} \sum_{k=1}^{N_l} x_{kl}, \\ y_l = \frac{1}{N_l} \sum_{k=1}^{N_l} y_{kl}, \end{cases} \quad (12)$$

where  $[x_l, y_l]^T$  is the average coordinates of the  $l$ th connected domain, for  $l = 1, 2, 3, \dots, L$ , and  $L$  denotes the number of connected domains (the total number of the extracted multipath



ghosts),  $[x_{kl}, y_{kl}]^T$  is the  $k$ th point of the  $l$ th connected domain,  $N_l$  denotes the number of pixels of the  $l$ th connected domain. To simplify the analysis, we define the  $L$  connected domains' tags as candidate multipath ghosts in one vector  $\mathbf{G}_{set}$ , i.e.

$$\mathbf{G}_{set} = [\mathbf{G}_1, \mathbf{G}_2, \mathbf{G}_l, \dots, \mathbf{G}_L], \quad (13)$$

where  $\mathbf{G}_l$  denotes the tag of the  $l$ th connected domain.

Note that if the location of a ghost caused by a path is known, the actual location of the target can be acquired. Due to the low energy attenuation and the certainty of the propagation process, ghost given rise to one-bounce reflection  $a_{22}$  as a typical ghost is considered to determine the actual location of the target in this paper.

According to the propagation path  $a_{22}$ , we know that the multipath ghost  $\mathbf{G}_{22} = [x_{G_{22}}, y_{G_{22}}]^T$  and the actual target  $W$  are symmetric with respect to Wall-2. Thus, based on the active area of hidden targets, the regions where multipath ghost  $G_{22}$  appear is as follows:

First, for the signal passing through path  $a_{22}$  before being reflected (see line  $OR_{a_{22}}$  in Fig. 2), the distribution range of  $G_{22}$  can be written as:

$$\Omega_1 : \left\{ \begin{array}{l} \bigcap_{m=1}^M \left\{ \mathbf{G}_{22} : y_{G_{22}} - \frac{(y_c - y_{tm})(x_{G_{22}} - x_c)}{x_c - x_{tm}} \leq y_c \right\} \\ \bigcap_{n=1}^N \left\{ \mathbf{G}_{22} : y_{G_{22}} - \frac{(y_c - y_{rn})(x_{G_{22}} - x_c)}{x_c - x_{rn}} \leq y_c \right\} \end{array} \right\}. \quad (14)$$

Likewise, after being reflected (see line  $W_1R_{a_{22}}$  in Fig. 2),

$$\Omega_2 : \left\{ \begin{array}{l} \bigcap_{m=1}^M \left\{ \mathbf{G}_{22} : y_{G_{22}} - \frac{(y_{tm} - y_c)(x_v + x_c)}{x_c - x_{tm}} \geq y_c \right\} \\ \bigcap_{n=1}^N \left\{ \mathbf{G}_{22} : y_{G_{22}} - \frac{(y_{rn} - y_c)(x_v + x_c)}{x_c - x_{rn}} \geq y_c \right\} \end{array} \right\}. \quad (15)$$

Then, for symmetric region of the NLOS,

$$\Omega_3 : \{ \mathbf{G}_{22} : D_2 \leq x_{G_{22}} \leq 2D_2 - D_1 \}, \quad (16)$$

where  $x_v = 2D_2 - x_{G_{22}}$ . Finally, the region of multipath ghost  $G_{22}$  may be represented in set form as

$$\mathbf{G}_{22} \in \{ \Omega_1 \cap \Omega_2 \cap \Omega_3 \}. \quad (17)$$

According to the analysis above,  $G_{22}$  is located in area  $\{ \Omega_1 \cap \Omega_2 \cap \Omega_3 \}$  when the position of the multi-channel UWB radar and positions of the wall are known. To simplify the analysis, we define a vector to represent that multipath ghost  $G_{22}$  from  $\mathbf{G}_{set}$  whose positions satisfy the Eq. (17), which is expressed as

$$\mathbf{U}_{set} = [\mathbf{U}_1, \mathbf{U}_2, \mathbf{U}_l, \dots, \mathbf{U}_{L_1}], L_1 \leq L, \quad (18)$$

where  $L_1$  is the total number of the candidates of  $\mathbf{G}_{22}$ .

### B. Multipath Ghosts Matching-Based Targets Localization

In this subsection, we introduce the multiple targets location method with the assumption that the position of the multipath ghost  $G_{22}$  are known in  $\mathbf{U}_{set}$ .

According to the known scene, for the  $l$ th candidate  $\mathbf{U}_l = [x_l, y_l]^T$  in  $\mathbf{U}_{set}$ , we define a candidate target vector, which is expressed as

$$\mathbf{U}_{candi} = [\mathbf{U}_{candi}^{(1)}, \mathbf{U}_{candi}^{(2)}, \mathbf{U}_{candi}^{(l)}, \dots, \mathbf{U}_{candi}^{(L_1)}], \quad (19)$$

that is, the coordinates of the candidate target  $\mathbf{U}_{candi}^{(l)} = [x_{candi}^{(l)}, y_{candi}^{(l)}]^T$  is calculated as

$$[x_{candi}^{(l)}, y_{candi}^{(l)}]^T = [2D_2 - x_l, y_l]^T. \quad (20)$$

It is assumed that the candidate target  $\mathbf{U}_{candi}^{(l)}$  is determined by the above calculation. Further, the corresponding time delay of the round-trip paths combined with the  $p$ th transmit path and the  $q$ th receive path can be calculated by

$$\tau_{p, \mathbf{U}_{candi}^{(l)}}^{(m)} = \frac{\|\mathbf{T}_m \mathbf{U}_l\|}{c}, \tau_{q, \mathbf{U}_{candi}^{(l)}}^{(n)} = \frac{\|\mathbf{R}_n \mathbf{U}_l\|}{c}. \quad (21)$$

Thus, the multipath ghosts corresponding to the candidate target  $\mathbf{U}_{candi}^{(l)}$  can be obtained. Similarly, we define a candidate multipath ghosts vector about candidate target vector  $\mathbf{U}_{candi}$ , denoted by

$$\mathbf{G}_{candi}^{(l)} = [\mathbf{G}_{candi,11}^{(l)}, \mathbf{G}_{candi,12}^{(l)}, \mathbf{G}_{candi,pq}^{(l)}, \dots, \mathbf{G}_{candi,44}^{(l)}]. \quad (22)$$

In order to calculate the positions of the candidate multipath ghosts with respect to different round-trip paths, the ellipse-cross-localization (ECL) technique is exploited [33]. Specifically, for a multipath ghost generated by a round-trip path, when there are  $M$  transmitting antennas and  $N$  receiving antennas,  $M \times N$  ellipses can be drawn. The multipath ghost will lie on both ellipses, so they intersect at a point which is the multipath ghost location.  $M \times N$  ellipses can intersect at multiple points, but in a practical scenario, only one intersection point corresponds to the multipath ghost of interest.

First, we define the propagation distance  $r_{i,pq}^{(l)}$  and  $r_{j,pq}^{(l)}$  of the  $i$ th and  $j$ th channels when the signals propagate through path  $a_{pq}$ . Noted that  $r_{i,pq}^{(l)}$  and  $r_{j,pq}^{(l)}$ ,  $p = q$  are the length of round-trip propagation path, which is calculated as

$$r_{i,11}^{(l)} = 2 \left\| \mathbf{U}_{candi}^{(l)} \mathbf{C} \right\| + \|\mathbf{T}_m \mathbf{C}\| + \|\mathbf{R}_n \mathbf{C}\|, \quad (23)$$

$$r_{i,22}^{(l)} = \|\mathbf{T}_m \mathbf{U}_l\| + \|\mathbf{R}_n \mathbf{U}_l\|, \quad (24)$$

$$r_{i,33}^{(l)} = \sqrt{\left( D_{v,1} + x_{candi}^{(l)} - x_{tm} \right)^2 + \left( y_{candi}^{(l)} - y_{tm} \right)^2} + \sqrt{\left( D_{v,1} + x_{candi}^{(l)} - x_{rn} \right)^2 + \left( y_{candi}^{(l)} - y_{rn} \right)^2} \quad (25)$$

and

$$r_{i,44}^{(l)} = \sqrt{\left( D_{v,2} - x_{candi}^{(l)} - x_{tm} \right)^2 + \left( y_{candi}^{(l)} - y_{tm} \right)^2} + \sqrt{\left( D_{v,2} - x_{candi}^{(l)} - x_{rn} \right)^2 + \left( y_{candi}^{(l)} - y_{rn} \right)^2}, \quad (26)$$

where  $i = m \times n$ ,  $D_{v,1} = 2D_2 - 2D_1$ ,  $D_{v,2} = 4D_2 - 2D_1$ .

In the L-shaped corner scenario, there are geometric relationships among different propagation paths. Hence, we can get the lengths of other combined propagation paths  $r_{i,pq}^{(l)}$  and  $r_{j,pq}^{(l)}$ ,  $p \neq q$ .

$$\begin{cases} r_{i,pq}^{(l)} = \frac{1}{2} (r_{i,pp}^{(l)} + r_{i,qq}^{(l)}), \\ r_{j,pq}^{(l)} = \frac{1}{2} (r_{j,pp}^{(l)} + r_{j,qq}^{(l)}). \end{cases} \quad (27)$$

Finally, the coordinates  $\mathbf{G}_{candi,pq}^{(l)} = [x_{candi,pq}^{(l)}, y_{candi,pq}^{(l)}]^T$  of the multipath ghost are given by

$$\begin{aligned} x_{candi,pq}^{(l)} &= \\ \frac{r_{i,pq}^{(l)} \left( (r_{j,pq}^{(l)})^2 - d_{j,pq}^2 \right) - r_{j,pq}^{(l)} \left( (r_{i,pq}^{(l)})^2 - d_{i,pq}^2 \right)}{2 \left( d_{j,pq} r_{i,pq}^{(l)} + d_{i,pq} r_{j,pq}^{(l)} \right)} \end{aligned} \quad (28)$$

and

$$\begin{aligned} y_{candi,pq}^{(l)} &= \\ \sqrt{\frac{\left[ \left( (r_{j,pq}^{(l)})^2 - d_{j,pq}^2 \right) \left( (r_{i,pq}^{(l)})^2 - d_{i,pq}^2 \right) \right] \cdot \left[ (d_{j,pq} + d_{i,pq})^2 - (r_{i,pq}^{(l)} - d_{i,pq})^2 \right]}{2 \left( d_{j,pq} r_{i,pq}^{(l)} + d_{i,pq} r_{j,pq}^{(l)} \right)}}, \end{aligned} \quad (29)$$

where  $i, j = 1, 2, \dots, M \times N$ ,  $i \neq j$ ,  $d_{i,pq}$  and  $d_{j,pq}$  represent the distance between the transmitting and receiving antennas of the  $i$ th and  $j$ th channel when signal propagates through path  $a_{pq}$ .

To evaluate the similarity between the candidate multipath ghosts and the actual multipath ghosts, we define two matching factors,  $\Phi^{(l)}$  and  $E^{(l)}$ , based on the relevance of  $\mathbf{G}_{set}$  and  $\mathbf{G}_{candi}^{(l)}$ , which are applied to identify the actual location of the target. Specifically, we have

$$\Phi^{(l)} = \sum_{p,q \in \{1,2,3,4\}, i \leq j} F_1 \left( \min_{\mathbf{G}_l \in \mathbf{G}_{set}} \left\| \mathbf{G}_{candi,pq}^{(l)} - \mathbf{G}_l \right\|_2 \right) \quad (30)$$

and

$$E^{(l)} = \sum_{p,q \in \{1,2,3,4\}, i \leq j} F_2 \left( \min_{\mathbf{G}_l \in \mathbf{G}_{set}} \left\| \mathbf{G}_{candi,pq}^{(l)} - \mathbf{G}_l \right\|_2 \right), \quad (31)$$

where  $\|\cdot\|_2$  represents the  $l_2$ -norm,  $F_1(\cdot)$  and  $F_2(\cdot)$  are defined as

$$F_1(x) = \begin{cases} 1, & x \leq T_b, \\ 0, & x > T_b, \end{cases} \quad (32)$$

and

$$F_2(x) = \begin{cases} x, & x \leq T_b, \\ 0, & x > T_b, \end{cases} \quad (33)$$

where  $T_b$  is a heuristic threshold with small value.

We repeat the above process for all the multipath ghosts in vector  $\mathbf{U}_{candi}$ . Then, the corresponding matching factors of each

---

**Algorithm 1:** Multiple Targets Localization Algorithm Based on Multipath Ghosts Matching.

---

**Input:**  $\mathbf{U}_{set}$ ,  $D_1$ ,  $D_2$ ,  $D_3$ ;

**Output:**  $\mathbf{U}_{real}^{(l)}$ ;

```

1  $x_{candi}^{(l)} = 2D_2 - x_l, y_{candi}^{(l)} = y_l$ ;
2 for  $l = 1 : L_1$  do
3   Obtain  $\tau_{p, \mathbf{U}_{candi}^{(l)}}^{(m)}$  and  $\tau_{q, \mathbf{U}_{candi}^{(l)}}^{(m)}$  based on (21);
4   Evaluate  $\mathbf{G}_{candi,pq}^{(l)}$  based on (28) and (29);
5   Compute  $\Phi^{(l)}$  and  $E^{(l)}$  based on (30) and (31);
6 end
7 if  $\exists \Phi^{(l)} : \max(\Phi)$  then
8    $\mathbf{U}_{real}^{(l)} = \mathbf{U}_{candi}^{(l)}$ ;
9 end
10 if  $\exists \Phi^{(l)} : \max(\Phi)$  then
11   Compute  $\min(E^{(l)})$  in vector  $\mathbf{E}$ ;
12    $\mathbf{U}_{real}^{(l)} = \mathbf{U}_{candi}^{(l)}$ ;
13 end
14 Derive the location of actual target  $\mathbf{U}_{real}^{(l)}$ ;
```

---

candidate target  $\mathbf{U}_{candi}^{(l)}$ ,  $l = 1, 2, \dots, L_1$  are obtained. Stacking these matching factors into two vectors  $\Phi$  and  $\mathbf{E}$ .

If candidate target  $\mathbf{U}_{candi}^{(l)}$  is a true target, all multipath ghosts produced by different round-trip paths will appear in the BP image, thus all the candidate multipath ghosts  $\mathbf{G}_{candi}^{(l)}$  will match correctly with the corresponding actual multipath ghosts  $\mathbf{G}_{set}$ , which means that  $\Phi^{(l)}$  will have the maximum value and  $E^{(l)}$  will have the minimum value compared to other candidate multipath ghosts. Conversely, the false targets will have a large matching-error.

Hence, the actual targets are identified by the following rules:

- If only one element in  $\Phi$  is equal to the maximum value  $\max(\Phi)$ , then, the corresponding candidate target  $\mathbf{U}_{candi}^{(l)}$  is selected as the actual target  $\mathbf{U}_{real}^{(l)}$ .
- If several elements in  $\Phi$  are equal to the maximum value of  $\max(\Phi)$ , the corresponding elements in  $\mathbf{E}$  will be compared and the minimum value  $\min(\mathbf{E})$  will be found. Further, the corresponding candidate target  $\mathbf{U}_{candi}^{(l)}$  of which is selected as the actual target  $\mathbf{U}_{real}^{(l)}$ .

In Algorithm 1, we give the detailed operations of the proposed algorithm.

### C. Trajectory Filtering

Moreover, due to the noise and clutters in the environment as well as the interference between multiple targets, some targets may be temporarily lost at some frames. Thus, the Kalman tracking filter algorithm is considered. Suppose that  $K$  periods of data have been collected in last subsection, let  $\hat{\mathbf{y}}(k)$ ,  $k = 1, 2, \dots, K$  denotes the estimated target location of the  $k$ th period, then, we construct the target state vector of the  $(k-1)$ th period as

$$\hat{\mathbf{Y}}(k-1) = \begin{bmatrix} \hat{\mathbf{y}}(k-1) \\ \mathbf{v} \end{bmatrix}, \quad (34)$$

where  $\mathbf{v}$  is the velocity of the target whose initial value can be estimated by the first two target positions. One-step-ahead estimator of target state is

$$\hat{\mathbf{Y}}(k|k-1) = \mathbf{F}\hat{\mathbf{Y}}(k-1) = \begin{bmatrix} \hat{\mathbf{y}}(k|k-1) \\ \mathbf{v} \end{bmatrix}, \quad (35)$$

where  $\hat{\mathbf{Y}}(k|k-1)$  and  $\hat{\mathbf{y}}(k|k-1)$  denote the one-step-ahead estimator and the predicted position separately at the  $k$ th period estimated from the  $(k-1)$ th period.  $\mathbf{F}$  represents the transition matrix.

In practice, the target moves with a relative low velocity comparing to the sampling rate of the radar system. The motion of targets can be described with the constant velocity model. In our experience, the result of Algorithm 1 will be fed into the Kalman filter to smooth the trajectory. The equations of the Kalman filter at the  $k$ th frame [34], are derived as follows:

$$\begin{aligned} \mathbf{P}(k|k-1) &= \mathbf{F}\mathbf{P}(k-1)\mathbf{F}^T + \mathbf{Q}_w, \\ \mathbf{K}(k) &= \mathbf{P}(k|k-1)\mathbf{H}^T[\mathbf{H}\mathbf{P}(k|k-1)\mathbf{H}^T + \mathbf{Q}_v]^{-1}, \\ \hat{\mathbf{Y}}(k) &= \hat{\mathbf{Y}}(k|k-1) + \mathbf{K}(k)[\hat{\mathbf{y}}(k) - \mathbf{H}\hat{\mathbf{Y}}(k|k-1)], \\ \mathbf{P}(k) &= [\mathbf{I} - \mathbf{K}(k)\mathbf{H}]\mathbf{P}(k|k-1), \end{aligned} \quad (36)$$

where  $\mathbf{P}(k|k-1)$  is a one-step-ahead error covariance matrix,  $\mathbf{P}(k)$  is the error autocorrelation matrix of state estimation,  $\mathbf{Q}_w$  denotes system state noise correlation matrix,  $\mathbf{Q}_v$  denotes measurement noise correlation matrix,  $\mathbf{K}(k)$  is the Kalman gain matrix,  $\mathbf{P}(k)$  is the error covariance matrix of state estimation,  $\mathbf{H}$  is observation matrix expressed as:

$$\mathbf{H} = \begin{bmatrix} 1 & 0 & 0 & 0 \\ 0 & 1 & 0 & 0 \end{bmatrix}. \quad (37)$$

#### IV. SIMULATION AND EXPERIMENTAL RESULTS

In this section, several simulation results and experimental results are provided to validate the effectiveness of the proposed multiple targets localization method based on multipath ghost image matching.

##### A. Simulation Results

The simulation data is derived from the Finite-Difference Time-Domain (FDTD) numerical method software gprMax [35]. A scenario containing an L-shaped corner with three walls is shown in Fig. 1.

The walls are homogenous with the relative permittivity  $\varepsilon_r = 6$  and conductivity  $\delta = 0.05$  S/m. The corner  $C$  is located at (1.5 m, 1.5 m) and  $D_1 = 1.5$  m,  $D_2 = 5$  m,  $D_3 = 1.5$  m. A multi-channel UWB radar array with two transmitting antennas and four receiving antennas is used to detect the targets. These two transmitting antennas are located at both ends of the array, 3.75 cm apart from the adjacent receiving antennas, and four receiving antennas are placed at equal intervals, spaced 7.5 cm apart.

The array center is located at (0.5 m, 0.9 m). The ricker waveform is employed as the transmitting signal with center

frequency  $f_c = 1$  GHz,  $B = 0.815$  GHz. These targets are set as homogenous cylinder with a radius of 0.2 m to simulate humans. The relative permittivity  $\varepsilon_r$  and conductivity  $\delta$  are 55 and 1.05 S/m, respectively. Besides that, the computing platform is a table computer with 2.8 GHz Intel(R) Core(TM) i5-8400 CPU and 12 GB of memory.

To evaluate the proposed method comprehensively, the influence of noise is also considered. If the EM wave propagation loss and reflection loss are  $\delta_1$  and  $\delta_2$  respectively, the relationship between the received echo power  $S'$  and the non-loss echo power  $S$  is expressed as [36]:

$$10 \lg \frac{S'}{S} = 2R\delta_1 + \delta_2, \quad (38)$$

where  $R$  is length of the wave propagation path. Further, the signal-to-noise ratios (SNR) as will be used further below is defined as the ratio of the target's power to the power of the noise for the raw echo of the single transmitting-receiving channel, given by

$$SNR = 10 \lg \frac{S'}{\sigma_n^2} = 10 \lg \frac{S\sigma'}{\sigma_n^2}, \quad (39)$$

where  $\sigma_n^2$  represents noise power,  $\sigma' = e^{(0.046\delta_1 R + 0.023\delta_2)}$ .

Four different simulation scenarios are considered in this subsection. Specifically, the first scenario *Case-1* and the second scenario *Case-2* contain a single target that moves along a curve route, where the SNR are set to 20 dB and 10 dB for all positions of target's trajectory respectively. The third scenario *Case-3* consists of two targets, one of which moves along a curve route and the other moves along a straight route. The moving route of the targets in *Case-4* is the same as *Case-3* but rough walls. The SNR of the *Case-3* and *Case-4* scenarios are 20 dB. For imaging, the surveillance region is discretized into numerous square pixels with a size of 0.04 m. The size of imaging zone is 10.5 m  $\times$  5.5 m. According to simulation targets and simulation scenarios, the threshold value  $T_b$  is set 0.5.

##### *Case-1: Single Target Moves in Scenario with 20 dB SNR*

In this simulation, a target moves from (2.15 m, 2.57 m) to (4.0 m, 2.8 m) along a curve route. The recorded data are corrupted with additive white Gaussian noise by assuming the SNR of 20 dB. To prove the abovementioned statement intuitively, in Fig. 5 (a), we give the range profile of channel-1 with respect to a common 72 periods of data.

The real types of different multipath have been marked. It's clear that most of the multipath propagation paths aforementioned appear in all periods, i.e.  $a_{11}$ ,  $a_{22}$ ,  $a_{24}$ ,  $a_{12}$ ,  $a_{23}$ ,  $a_{34}$ ,  $a_{13}$  and  $a_{33}$ . In addition, the types of the some multipaths have not been found in the range profile, for example,  $a_{14}$ ,  $a_{34}$  and  $a_{44}$ . This has mainly been caused by the aliasing between paths and the attenuation of reflection. Especially, the echo amplitudes derived from some high-order reflections such as  $a_{34}$  and  $a_{44}$  are lower than noise, which may result in some missed detections. Note that the positions and the amplitudes of these paths vary with the target location, leading to the difficulty to distinguish these paths and apply them to obtain the target's position accurately.

Based on the range profile, the position of the single target can be calculated by using the proposed algorithm. Fig. 5 (b)-(d)

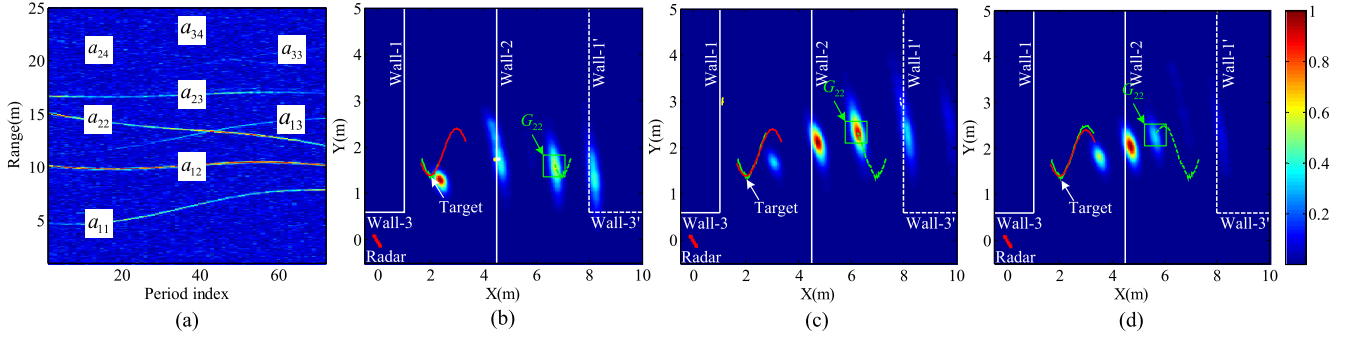


Fig. 5. Simulation results of single target moves along a curve route in the L-shaped scenario with 20 dB SNR. (a) Range profile plane for single target. (b) Positioning result of the 25th period. (c) Positioning result of the 45th period. (d) Positioning result of the 72th period.

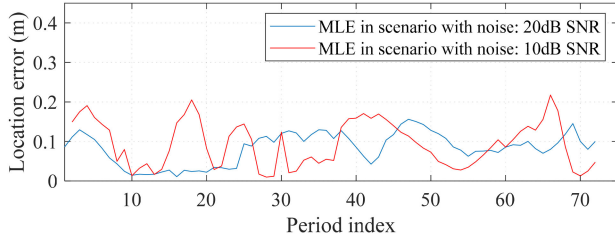


Fig. 6. MLE curves of the single moving target in the scenario with different noise.

show the positioning results with respect to three different periods. In each figure, the red solid curve denotes the real movement route of the target, while the green solid line and green dotted line represent the moving route and mirror symmetry moving route obtained by the method we proposed, respectively. In addition, to facilitate the observation, the positions of the actual wall and the positions of the symmetrical wall are marked on these figures.

We can see that multipath ghosts  $G_{11}, G_{12}, G_{22}$  and  $G_{23}$  are found in the imaging results. Due to noise interference, a false alarm (lines in other colors) appears in both Fig. 5(b) and Fig. 5(c). But beyond that, other multipath ghosts are also used to calculate the matching factors  $\Phi$  and  $E$ . Kalman filter algorithm is also exploited, thus a smooth and stable target trajectory is successfully obtained.

To quantitatively evaluate the localization accuracy of the proposed method, the mean localization error (MLE) between the target's actual positions and the estimated positions in each period is given by:

$$MLE = \frac{1}{N_w} \sum_{\rho=1}^{N_w} \sqrt{(x_\rho - \hat{x}_\rho)^2 + (y_\rho - \hat{y}_\rho)^2}. \quad (40)$$

where  $N_w$  is the total number of targets,  $x_\rho$  and  $y_\rho$  are the coordinates of the actual target positions,  $\hat{x}_\rho$  and  $\hat{y}_\rho$  are the coordinates of the estimated target positions, and  $\rho$  is the target number.

Fig. 6 shows the MLE curve of single moving target in the L-shaped scenario with different noise value, in which the noise of blue dotted line and red solid line are 20 dB and 10 dB respectively. For *Case-1* (SNR = 20 dB), although the location

error fluctuates in different periods, the maximum value of the MLE is only 0.17 m and the minimum value of the MLE is 0.01 m. Considering the size of the target itself, the error value is within the acceptable range, which proves the effectiveness of the algorithm. Thus, the proposed method can deal with the multitarget scenario.

#### Case-2: Single Target Moves in Scenario with 10 dB SNR

In this simulation, the target maintains the same motion route as *Case-1*. However, SNR is 10 dB. Fig. 7 (a) shows the range profile of channel-1 with respect to a common 72 periods of data. Only six multipaths have been found, such as  $a_{11}, a_{22}, a_{24}, a_{12}, a_{23}$  and  $a_{13}$ . Due to the influence of strong noise,  $a_{33}$  and  $a_{34}$  in Fig. 5 (a) cannot be observed in Fig. 7 (a). Moreover, compared with the range profile in Fig. 5 (a), there are many multipaths with weaker amplitude than noise in Fig. 7 (a), which results in some multipath ghosts being submerged by noise.

Fig. 7 (b)–(d) show the positioning results of a moving single target with respect to three different periods when SNR = 10 dB. Note that the representation of line symbols are consistent with *Case-1*. It can be seen that there are a large number of ghosts caused by noise in the imaging region with different periods. Fortunately, the amplitudes of multipath ghost caused by path  $a_{11}, a_{22}$  and  $a_{24}$  are still stronger than that of noise, which can be extracted to associate the position of real target. Similarly, the results of Fig. 7(b) and Fig. 7(c) contain three and one false alarms, respectively. Although the target motion trajectory can still be obtained by the proposed algorithm, the jitter of the obtained track is larger than that of Fig. 5.

The MLE curve of single moving target is shown in Fig. 6, where the red line represents the positioning error when SNR = 10 dB. In this curve, although the error curve fluctuates greatly, the maximum value of the MLE is only 0.22 m and the minimum value of the MLE is 0.01 m, which indicates that the algorithm is still effective at low SNR. Thus, the proposed approach can be applied to obtain the coordinates of a moving target, which is concealed behind an L-shaped corner.

#### Case-3: Two Moving Targets in Scenario with Smooth Walls

In this simulation, two moving targets are considered to verify the location performance of the proposed algorithm. One target named Target-A moves from (2.00 m, 1.90 m) to (2.05 m, 3.11 m) along a curve route and the other target named Target-B moves from (2.50 m, 2.30 m) to (3.57 m, 3.15 m) along a straight route.



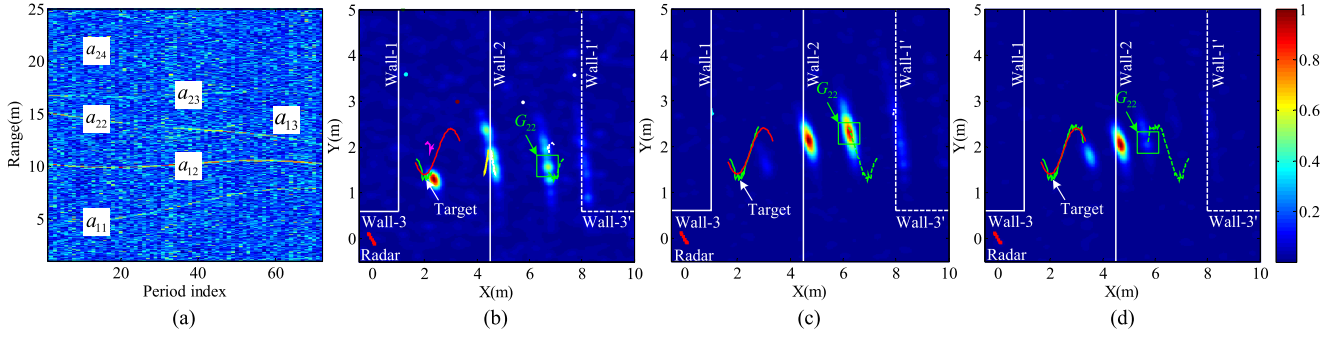


Fig. 7. Simulation results of single target moves along a curve route in the L-shaped scenario with 10 dB SNR. (a) Range profile plane for single target. (b) Positioning result of the 25th period. (c) Positioning result of the 45th period. (d) Positioning result of the 72th period.

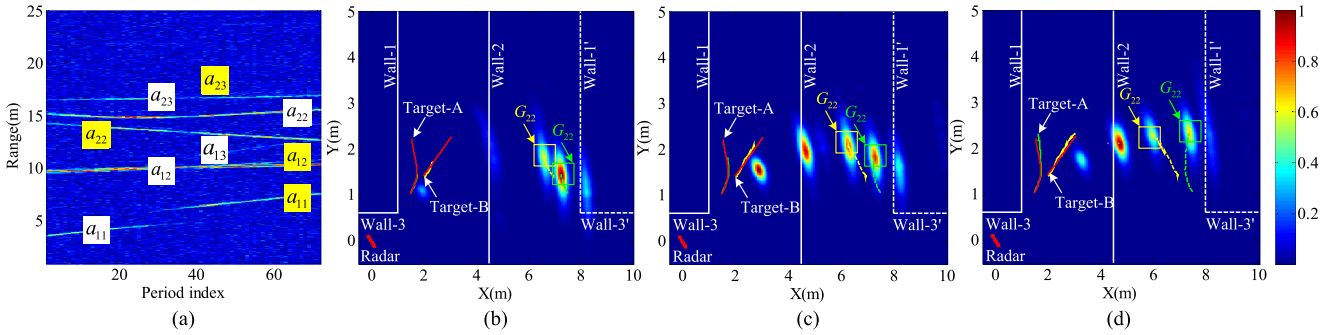


Fig. 8. Simulation results of two moving targets in the L-shaped scenario with smooth walls (SNR = 20 dB). (a) Range profile plane for two targets. (b) Positioning result of the 25th period. (c) Positioning result of the 45th period. (d) Positioning result of the 72th period.

Additionally, additive white gaussian noise is added to the signal, which makes the SNR = 20 dB.

Fig. 8 (a) shows the range profile of channel-1 with respect to a common 72 periods of data. The real types of different multipaths of Target-A and Target-B have been marked by the white marks and the yellow marks, respectively. It is clear that most of the multipaths of the two targets appear, but the types of multipaths of Target-B are obviously less than that of Target-A. Due to the relative location of the two targets in simulation, some multipaths of the two targets are similar in distance, such as path  $a_{12}$  of the Target-A and path  $a_{13}$  of the Target-B, while some multipaths differ greatly in distance, such as  $a_{11}$  of the Target-A and  $a_{23}$  of the Target-B. Furthermore, some types of multipaths do not exist, which may be caused by occlusion of the targets.

Note that the irregular distribution of these multipaths in the range profile will lead to the difficulty of multiple targets positioning. For multiple targets, although the types of multipaths can not be resolved through one-dimensional range profile, the distribution of multipath ghosts are related to the targets location in the two-dimensional radar image.

Thus, based on the proposed method, we obtain the localization results of the targets related to three different periods as shown in Fig. 8 (b)-(d). Specifically, the green solid line and green dotted line represent the moving route and mirror symmetry moving route of Target-A obtained by the method we proposed, respectively. The yellow solid line and yellow dotted

line represent the moving route and mirror symmetry moving route of Target-B obtained by the proposed method, respectively. In these results, we have marked the actual locations of two targets in the red solid line. We can see that the ghosts of different targets can be extracted to construct the corresponding matching vectors  $\Phi$  and  $\mathbf{E}$  in the proposed algorithm, for instance,  $G_{11}$ ,  $G_{12}$  and  $G_{22}$ . Overall, the proposed method can effectively obtain the location of multiple targets.

Similarly, MLE is used to evaluate localization accuracy for localization of the multiple targets. Specifically, in Fig. 9 (a), the blue line indicates the location error of Target-A, while the blue line indicates the location error of Target-B in Fig. 9 (b). The maximum value of the MLE of Target-A and Target-B are 0.25 m and 0.21 m, respectively. Compared to the MLE in single target scene, due to mutual interference between multiple targets, the location errors are generally larger in Fig. 9. However, considering the size of the target itself, the maximum error is also within an acceptable level.

#### Case-4: Two Moving Targets in Scenario with Rough Walls

In this simulation, the moving routes of the targets and the SNR (20 dB) are set to be the same as Case-3. Multiple targets localization in non-ideal scenarios is considered, where roughness is taken into account when the surface of walls are not smooth. An simplified investigation to approximate the impact of wall roughness is provided. We use random perturbations to model roughness, which is first proposed by [37]. Specifically, assume that the wall consists of  $N_{wall}$  points, denoted by

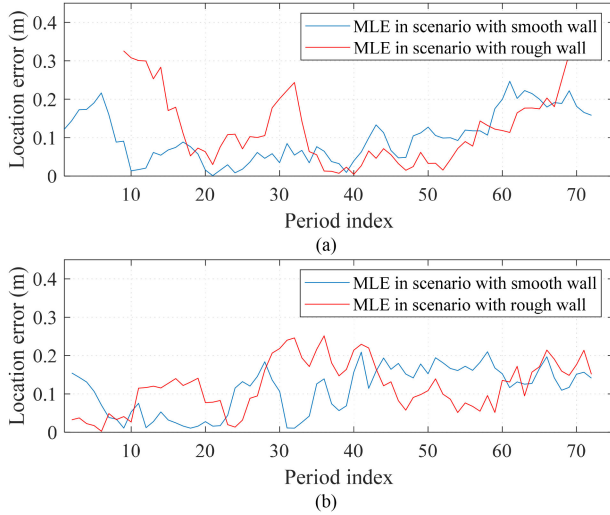


Fig. 9. MLE curves of two moving targets in the scenario with different walls. (a) MLE curves of the Target-A. (b) MLE curves of the Target-B.

$\mathbf{SR}_n = [x_n, y_n]^T, n = 1, 2, \dots, N_{wall}$ . Then, the  $x$ -coordinate is modeled as a normal distribution, in which the probability density function (PDF) is expressed as:

$$f(x_n) = \frac{1}{\sqrt{2\pi}\mu\lambda_c} \exp\left(-\frac{(x_n - x_b)^2}{2(\mu\lambda_c)^2}\right), \quad (41)$$

where  $x_b$  and  $\mu\lambda_c$  represent the mean and standard deviation, respectively. Note that  $x_b$  is the baseline of the wall, its distance to Wall-1 a and Wall-2 is  $D_1'$  and  $D_2'$  respectively,  $\lambda_c$  is the corresponding wavelength of the center frequency and  $\mu$  is the roughness percentage.

According to the above roughness analysis, the modeling wall data is imported into gprMax EM simulation software to obtain the simulation data in the non-ideal scenario. Without loss of generality, the roughness percentage  $\mu = 5\%$  which means the standard deviation of  $x_n$  is 0.785 cm and the difference of the two adjacent  $y_n$  is 1.51 cm. In Fig. 10 (a), we give the range profile of channel-1 with respect to a common 72 periods of data. Compared with Fig. 8 (a), the multipath types of different targets have not changed in Fig. 10 (a), but these range trajectories have been disturbed and expanded.

According to the range profile, the positions of the multiple targets can be calculated by using the proposed algorithm. Fig. 10 (b)-(d) show localization results of two moving targets in non-ideal scenario. In these figures, the actual locations of two targets have been marked by the red solid lines. As with Fig. 8, the green solid line and green dotted line represent the moving route and mirror symmetry moving route of Target-A obtained by the method we proposed, respectively. The yellow solid line and yellow dotted line represent the moving route and mirror symmetry moving route of Target-B obtained by the proposed method, respectively.

In general, if the surface of the wall is not smooth, the signal high-order reflection such as  $a_{33}$  and  $a_{34}$  will disappear or weaken. It can be seen that several typical multipath ghosts still

exist, but the positions are biased. However, compared with the results of Fig. 8 (b)-(d), the multipath ghosts  $G_{22}$  are missed due to the influence of the walls roughness in Fig. 10 (b)-(d). From both ends of the location routes in Fig. 10, we can find that the location error of Target-A is larger when the target is close to the roughness wall. This is because when the target is closer to the wall, the propagation deviation caused by the rough wall between different transmitting-receiving channels is greater, resulting in a larger imaging error in the BP image. Fig. 9 shows the corresponding MLE curves of two moving targets in the non-ideal scenario, where the red line indicates the location error of Target-A in Fig. 9 (a), while the red line indicates the location error of Target-B in Fig. 9 (b). The maximum value of the MLE of Target-A and Target-B are 0.32 m and 0.25 m, respectively.

For comparison and analysis, the simulation results of the four cases are shown in Table I. In most of the periods, the target location error is small enough to be allowed. Simultaneously, two matching factors with a heuristic threshold  $T_b$  are designed to evaluate the similarity between the candidate multipath ghosts and the actual multipath ghosts in our proposed method. In addition, two decision rules are also designed to handle some missed detections. Thus, all the targets are located successfully. Thus, the proposed approach can be applied to obtain the coordinates of moving multiple targets behind an L-shaped corner where roughness is considered.

## B. Experimental Results

To further validate the proposed algorithm, we also perform several experiments by exploiting a multi-channel UWB radar with two transmitting antennas and four receiving antennas which were constructed at the campus of University of Electronic Science and Technology of China. The stepped-frequency continuous waveform is employed as the transmitted signal. Specifically, the detailed parameters of the multi-channel UWB radar system are listed in Table II.

The radar equipment and experimental scenario are depicted as Fig. 11 and Fig. 12, respectively, where the height from the ceiling to the ground is 3.25 m and the width of the corridor is 6.42 m. The two transmitting antennas are located at  $(-0.42 \text{ m}, -0.53 \text{ m})$  and  $(-0.39 \text{ m}, -0.60 \text{ m})$ , and the receiving antennas are placed from  $(-0.51 \text{ m}, -0.37 \text{ m})$  to  $(-0.31 \text{ m}, -0.76 \text{ m})$  with the space of 0.075 m. The horizontal beam width and the vertical beam width of the UWB radar we use are set to  $90^\circ$  and  $30^\circ$  to cover the two main propagation paths of diffraction and reflection, while minimizing the reflection from the ceiling and the ground. In addition, all of the antennas are faced toward the corner directly with a height of 1.1 m. For imaging, the surveillance region is discretized into square pixels with a size of 0.05 m. The size of the imaging zone is  $14.5 \text{ m} \times 12.5 \text{ m}$ . The human will inevitably have micro movements during the data collection, such as waving hands, shaking head, etc. Thus, the threshold value  $T_b$  is set 0.8. In the following, two experiments with different numbers of targets are conducted.

### Case-1: Single Micro-Motion Target

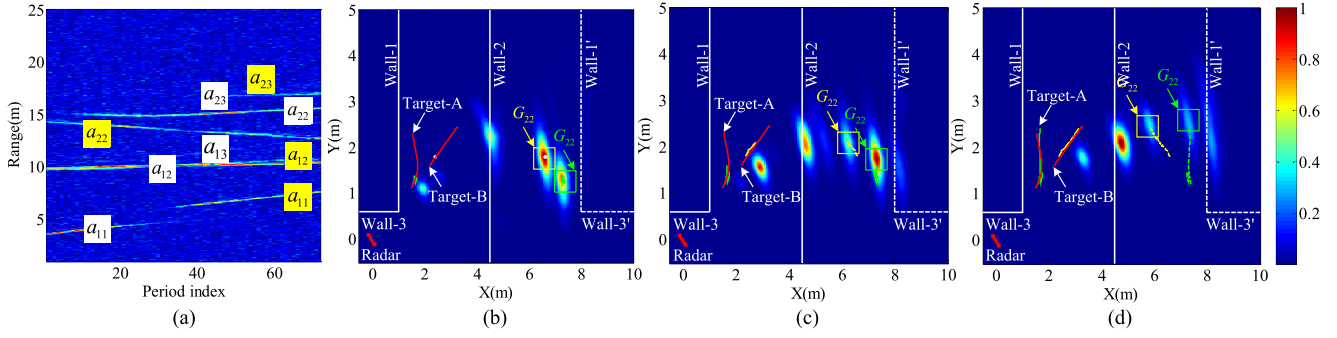


Fig. 10. Simulation results of two moving targets in the L-shaped scenario with rough walls (SNR = 20 dB). (a) Range profile plane for two targets. (b) Positioning result of the 25th period. (c) Positioning result of the 45th period. (d) Positioning result of the 72nd period.

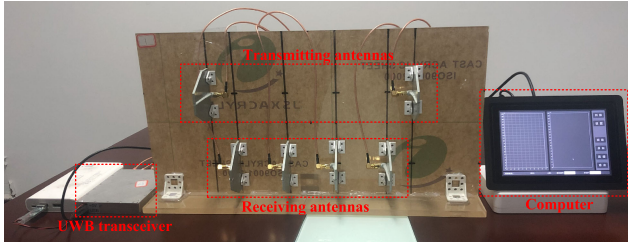


Fig. 11. Multi-channel UWB radar system. The experimental measuring equipment consists of UWB transceiver, transmitting antennas, receiving antennas and computer.



Fig. 12. Photos of the experimental scenario. Case-1: single micro-motion target scenario. Case-2: two micro-motion targets scenario.

In the first experiment, to ensure the target is located at the NLOS area completely, a person stands at the position (1.7 m, 5.4 m) at first, as shown in Case-1 of Fig. 12. Then, he swayed back and forth with a small range during the data collection, in which 500 periods of data were collected. As illustrated in Fig. 13 (a), the range profile of channel-1 with respect to all periods of data is shown. It can be seen that there are three multipath range trajectories, e.g.,  $a_{11}$ ,  $a_{12}$  and  $a_{22}$ . Among them,  $a_{22}$  has the strongest amplitude. In addition, we find that the path relationship described in the proposed algorithm is satisfied by

calculating the length of paths  $a_{11}$ ,  $a_{12}$  and  $a_{22}$ , as shown in Eq. (27).

Based on the range profile, the position of the single target can be calculated by using the proposed algorithm. Fig. 13 (b)-(d) show the positioning results with respect to three different periods. In each figure, the green point and yellow point represent the target position and mirror symmetry position of the target obtained by the method we proposed, respectively, while other color points indicate the false locating points in these figures. Specifically, a total of four false alarms appeared in the positioning results. It is worth noting that these false locating points only appear in some periods or around the target.

Different from the simulation, in the real data, the detected target is no longer a regular shape, but an irregular human target. Therefore, the size of human body needs to be considered. The body movements will cause other chaotic returns. Based on actual conditions, an appropriate threshold  $T_b$  is designed to obtain the corresponding matching factor  $\Phi$  and  $\mathbf{E}$  in our proposed method. In addition, the filtering algorithm can also remove some missed detections.

In addition, some ground or ceiling reflection signals may be added into returns in the real data. Thus, some ghosts caused by the reflected path echoes from the ground and ceiling may appear in the image. However, note that the proposed algorithm focuses on the locations matching relationship between ghosts caused by wall reflection paths, while other ghosts caused by ground or ceiling reflections do not satisfy the target matching relationship. Therefore, ground or ceiling reflection echoes will not substantially affect the acquisition of the targets position.

#### Case-2: Two Micro-Motion Targets

In the second experiment, two micro-motion targets are considered, in which Target-A and Target-B are located at (1.1 m, 3.7 m) and (2.95 m, 7.1 m) in the NLOS area, respectively, as shown in Case-2 of Fig. 12. A total of 200 periods of data were collected when the targets swayed back and forth with a small range. Similarly, Fig. 14 (a) shows the corresponding range profiles. We can clearly see that different multipath of different targets are marked with different colors. Specifically, white squares represent Target-A, while yellow squares represent Target-B. The multipath of different targets still satisfies the relation of Eq. (27). Moreover, due to the close distance between



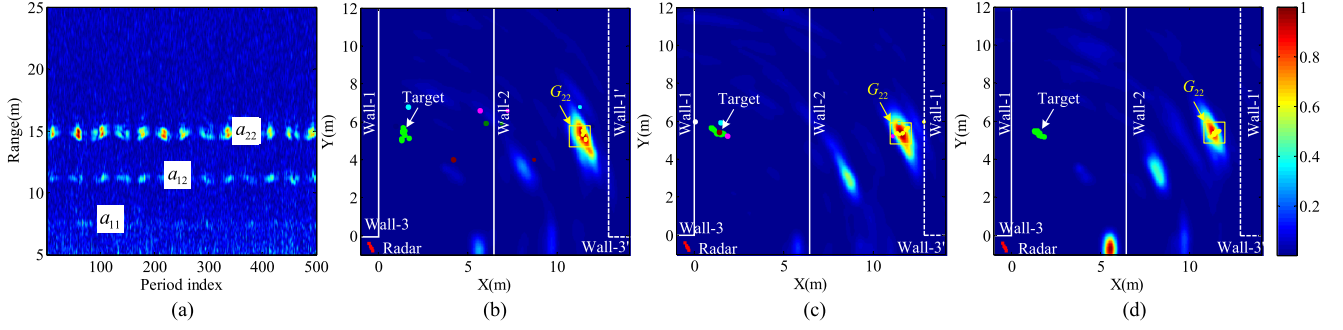


Fig. 13. Processing results of the single micro-motion target in the L-shaped scenario with real data. (a) Range profile plane for single target. (b) Positioning result of the 25th period. (c) Positioning result of the 50th period. (d) Positioning result of the 95th period.

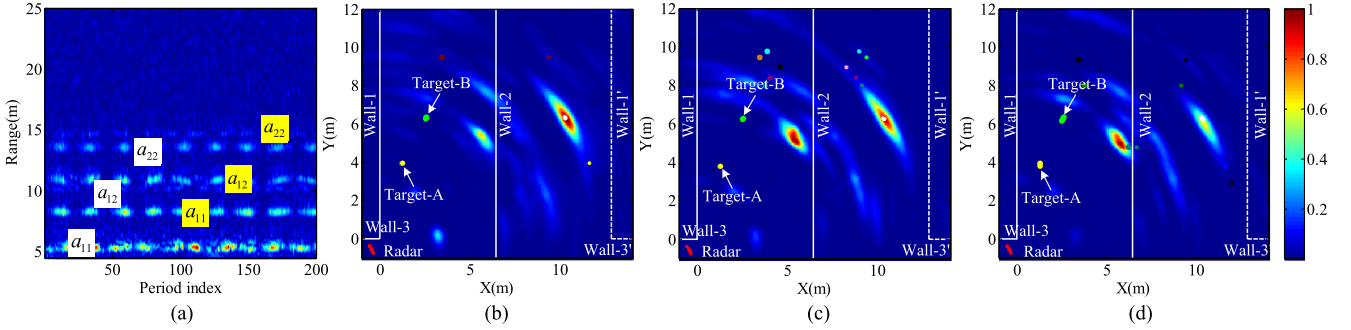


Fig. 14. Processing results of two micro-motion targets in the L-shaped scenario with real data. (a) Range profile plane for two targets. (b) Positioning result of the 12th period. (c) Positioning result of the 60th period. (d) Positioning result of the 90th period.

different multipath, some multipath ghosts may be hard to be separated in the radar images.

After the processing of the proposed method, the positions of targets are obtained, as shown in Fig. 14 (b)-(d). Specifically, the yellow points and blue points represent the position and mirror symmetry target of Target-A obtained by the method we proposed, respectively. The green points and white points represent the position and mirror symmetry target of Target-B obtained by the proposed method, respectively. Furthermore, other color points represent false target locations. Due to inter-target interference and noise, five false targets were found in the positioning results. These false targets caused by environment noise and imaging error exist randomly at different periods.

Different from Fig. 14, in the case of multiple targets, the interference between targets must be considered, which is also the reason why Fig. 14 has more wrong positioning points than Fig. 14. Fortunately, some of these false targets can be removed through the constraints of decision rules and Kalman filtering, so that not to affect the judgment of real targets.

Compared with the simulation results, it can be seen that more types of multipath ghosts are existing in the simulation results than real data. On the one hand, the resolution of the radar is limited, causing some multipath to be overlapped. On the other hand, the more-bounce energy in the measured environment is severely attenuated, and only the obvious diffraction and one-bounce are included in the returns. According to the proposed targets localization method based on multipath ghosts image

matching, even if only multipath related to diffraction and one reflection are detected, the image matching relationship can be established and the targets can still be located.

In fact, if more types of multipath ghosts are extracted by adjusting the radar resolution and transmission power, it will improve the positioning performance of the proposed algorithm. Furthermore, considering the expansion characteristics and the body swing of the human target, the above analyzed errors are acceptable in practice. Overall, the proposed algorithm can achieve good NLOS targets positioning performance in the L-shaped corner scenario.

## V. CONCLUSION

A novel localization algorithm of the multi-channel UWB imaging radar has been designed to implement localization of hidden multiple targets via NLOS signals. The application of the proposed algorithm makes it feasible to implement multiple targets localization in an L-shaped corner environment. First, a multipath propagation model of the multiple targets has been established and the characters of the multipath signals received by multi-channel UWB radar have been analysed. Then, a moving multiple targets localization algorithm by matching the multipath ghosts after applying the BP imaging algorithm has been proposed. Finally, several simulations and real data results validate the effectiveness of the proposed algorithm.



The proposed method can cope with the case when some missed detections of multipath ghosts appear, caused by such as noise, surface roughness of the wall, etc. If the building structure information is known, the proposed algorithm is not limited to the L-shaped scenario, it can also be transposed to the common cross shaped scenario. However, considering the complexity of the echo signal when the targets are far away in the corridor, only first order reflection is used as a hypothetical condition to perform target positioning. Thus, they represent a remaining challenge to be solved. Our ongoing work will be focused on long-distance targets detection in the corridor. In future work, the influence of the precision accuracy about the scene will also be analyzed. We also plan to carry out experiments for more complex scenes and different target (e.g., bicycles, cars) by using machine learning.

## REFERENCES

- [1] T. Jin, B. Chen, and Z. Zhou, "Image-domain estimation of wall parameters for autofocus of through-the-wall SAR imagery," *IEEE Trans. Geosci. Remote Sens.*, vol. 51, no. 3, pp. 1836–1843, Aug. 2012.
- [2] S. Guo, G. Cui, L. Kong, and X. Yang, "An imaging dictionary based multipath suppression algorithm for through-wall radar imaging," *IEEE Trans. Aerosp. Electron. Syst.*, vol. 54, no. 1, pp. 269–283, Sep. 2018.
- [3] H. Li, G. Cui, L. Kong, G. Chen, M. Wang, and S. Guo, "Robust human targets tracking for MIMO through-wall radar via multi-algorithm fusion," *IEEE J. Sel. Top. Appl. Earth Observ. Remote Sens.*, vol. 12, no. 4, pp. 1154–1164, Mar. 2019.
- [4] P. Ho and J. Chen, "WiSafe: Wifi pedestrian collision avoidance system," *IEEE Trans. Veh. Technol.*, vol. 66, no. 6, pp. 4564–4578, Jun. 2017.
- [5] N. Scheiner *et al.*, "Seeing around street corners: Non-line-of-sight detection and tracking in-the-wild using doppler radar," in *Proc. IEEE Conf. Comput. Vis. Pattern Recognit.*, Los Angeles, CA, USA, 2020, pp. 2068–2077.
- [6] S. Sun, A. P. Petropulu, and H. V. Poor, "MIMO radar for advanced driver-assistance systems and autonomous driving: Advantages and challenges," *IEEE Signal Process. Mag.*, vol. 37, no. 4, pp. 98–117, Jul. 2020.
- [7] D. Solomitskii, C. B. Barneto, M. Turunen, M. Alln, Y. Koucheryav and M. Valkama, "Millimeter-wave automotive radar scheme with passive reflector for blind corner conditions," in *Proc. Eur. Conf. Antennas Propag.*, 2020, pp. 1–5.
- [8] K. Thai *et al.*, "Around-the-corner radar: Detection and localization of a target in non-line of sight," in *Proc. IEEE Radar Conf.*, 2017, pp. 0842–0847.
- [9] R. Zetik, M. Roding, and R. S. Thoma, "UWB localization of moving targets in shadowed regions," in *Proc. Eur. Conf. Antennas Propag.*, 2012, pp. 1729–1732.
- [10] P. Setlur, T. Negishi, N. Devroye, and D. Erricolo, "Multipath exploitation in non-los urban synthetic aperture radar," *IEEE J. Sel. Top. Signal Process.*, vol. 8, no. 1, pp. 137–152, Feb. 2013.
- [11] S. Fujita, T. Sakamoto, and T. Sato, "An accurate UWB radar imaging method using indoor multipath echoes for targets in shadow regions," in *Proc. Int. Conf. Indoor Positioning Indoor Navigation*, 2010, pp. 1729–1732.
- [12] G. Gennarelli, G. Riccio, R. Solimene, and F. Soldovieri, "Radar imaging through a building corner," *IEEE Trans. Geosci. Remote Sens.*, vol. 52, no. 10, pp. 6750–6761, Feb. 2014.
- [13] R. Linnehan and J. Schindler, "Multistatic scattering from moving targets in multipath environments," in *Proc. IEEE Radar Conf.*, 2009, pp. 1–6.
- [14] D. Deiana, A. S. Kossen, and W. L. van Rossum, "Multipath exploitation in an urban environment using a MIMO surveillance radar," in *Proc. Int. Radar Symp.*, 2010, pp. 1–4.
- [15] A. Sume *et al.*, "Radar detection of moving targets behind corners," *IEEE Trans. Geosci. Remote Sens.*, vol. 49, no. 6, pp. 2259–2267, Jun. 2011.
- [16] M. Gustafsson, A. Andersson, T. Johansson, S. Nilsson, A. Sume, and A. Orbom, "Extraction of human micro-doppler signature in an urban environment using a "sensing-behind-the-corner" radar," *IEEE Geosci. Remote Sens. Lett.*, vol. 13, no. 2, pp. 187–191, Feb. 2016.
- [17] T. Johansson *et al.*, "Radar measurements of moving objects around corners in a realistic scene," in *Proc. SPIE*, vol. 9077, Art. no. 90771Q, May 2014.
- [18] T. Johansson, A. Andersson, M. Gustafsson, and S. Nilsson, "Positioning of moving non-line-of-sight targets behind a corner," in *Proc. Eur. Radar Conf.*, 2016, pp. 181–184.
- [19] R. Zetik, M. Eschrich, S. Jovanoska, and R. Thoma, "Looking behind a corner using multipath-exploiting UWB radar," *IEEE Trans. Aerosp. Electron. Syst.*, vol. 51, no. 3, pp. 1916–1926, Jul. 2015.
- [20] K. Thai, O. Rabaste, J. Bosse, and T. Chonavel, "GLRT particle filter for tracking NLOS target in around-the-corner radar," in *Proc. IEEE Int. ASSP Conf.*, 2018, pp. 3216–3220.
- [21] K. Thai, O. Rabaste, J. Bosse, and D. Poullin, "Detection-localization algorithms in the around-the-corner radar problem," *IEEE Trans. Aerosp. Electron. Syst.*, vol. 55, no. 6, pp. 2658–2673, Dec. 2019.
- [22] S. Guo, Q. Zhao, G. Cui, S. Li, L. Kong, and X. Yang, "Behind corner targets location using small aperture millimeter wave radar in NLOS urban environment," *IEEE J. Sel. Top. Appl. Earth Observ. Remote Sens.*, vol. 13, pp. 460–470, Jan. 2020.
- [23] X. Yang, S. Fan, S. Guo, S. Li, G. Cui, and W. Zhang, "NLOS target localization behind an L-shaped corner with an L-band UWB radar," *IEEE Access*, vol. 8, pp. 31270–31286, Feb. 2020.
- [24] S. Li, G. Cui, S. Guo, C. Jia, L. Kong, and X. Yang, "On the electromagnetic diffraction propagation model and applications," *IEEE J. Sel. Top. Appl. Earth Observ. Remote Sens.*, vol. 13, pp. 884–895, Feb. 2020.
- [25] S. Fan, G. Cui, S. Guo, L. Kong, X. Yang, and X. Yuan, "Corner target positioning with unknown walls' positions," *J. Eng.*, vol. 19, pp. 6143–6146, Oct. 2019.
- [26] S. Guo, S. Li, G. Cui, S. Fan, L. Kong, and X. Yang, "MIMO radar localization of targets behind l-shaped corners," in *Proc. IEEE Sensor Array Multichannel Signal Process.*, 2020, pp. 1–4.
- [27] M. Wang, G. Cui, W. Yi, L. Kong, X. Yang, and L. Yuan, "Time-division MIMO through-the-wall radar imaging behind multiple walls," in *Proc. IEEE Radar Conf.*, 2010, pp. 15–17.
- [28] M. Jacob, S. Priebe, R. Dickhoff, T. Ostmann, T. Schrader, and T. Kurner, "Diffraction in mm and sub-mm wave indoor propagation channels," *IEEE Trans. Microw. Theory Tech.*, vol. 60, no. 3, pp. 833–844, Jan. 2012.
- [29] H. Brunzell, "Detection of shallowly buried objects using impulse radar," *IEEE Trans. Geosci. Remote Sens.*, vol. 37, no. 2, pp. 875–886, Mar. 1999.
- [30] F. Ahmad, M. G. Amin, and S. A. Kassam, "Synthetic aperture beamformer for imaging through a dielectric wall," *IEEE Trans. Aerosp. Electron. Syst.*, vol. 41, no. 1, pp. 271–283, Jan. 2005.
- [31] S. Haykin, *Digital Communication Systems*. New York, NY, USA: Wiley, 2014.
- [32] S. Guo, G. Cui, M. Wang, L. Kong, and X. Yang, "Similarity-based multipath suppression algorithm for through-wall imaging radar," *IET Radar Sonar Navigation*, vol. 11, no. 7, pp. 1041–1050, Jul. 2017.
- [33] R. Amiri, F. Behnia, and M. A. M. Sadr, "Exact solution for elliptic localization in distributed MIMO radar systems," *IEEE Trans. Veh. Technol.*, vol. 27, no. 2, pp. 1075–1086, Oct. 2017.
- [34] Y. Zhang, M. G. Amin, and F. Ahmad, "Application of time-frequency analysis and Kalman filter to range estimation of targets in enclosed structures," in *Proc. IEEE Radar Conf.*, 2008, pp. 1–4.
- [35] C. Warren *et al.*, "A CUDA-based GPU engine for gprMax: Open source FDTD electromagnetic simulation software," *Comput. Phys. Commun.*, vol. 237, pp. 208–218, Apr. 2019.
- [36] M. A. Richards, *Fundamentals of Radar Signal Processing*. New York, NY, USA: McGraw-Hill, 2005.
- [37] S. O. Rice, "Reflection of electromagnetic waves from slightly rough surfaces," *Commun. Pure Appl. Math.*, vol. 4, no. 2/3, pp. 369–373, Jul. 1956.



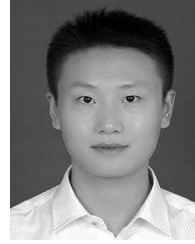
**Songlin Li** received the B.S. degree from the Chengdu University of Technology, Chengdu, China, in 2018. He is currently working toward the M.S. degree with the School of Information and Communication Engineering, University of Electronic Science and Technology of China, Chengdu, China.

His research interests include NLOS target detection in urban environment.



**Shisheng Guo** (Member, IEEE) received the B.S. degree in communication engineering from the Nanchang Hangkong University, Nanchang, China, in 2013, and the Ph.D. degree in signal and information processing from the University of Electronic Science and Technology of China (UESTC), Chengdu, China, in 2019.

He is currently an Associate Researcher with the School of Information and Communication Engineering, UESTC. His research interests include through-the-wall radar imaging, signal analysis and NLOS target detection.



**Chao Jia** received the M.S.E.E. degree from the University of Electronic Science and Technology of China (UESTC), Chengdu, China, in 2013. He is currently working toward the D.E. degree with the School of Information and Communication Engineering, UESTC.

His research interests include NLOS target detection in urban environment and radar signal processing.



**Jiahui Chen** received the B.S. degree in electronic information science and technology from the North China Electric Power University, Baoding, China, in 2018. He is currently working toward the Ph.D. degree with the School of Information and Communication Engineering from the University of Electronic Science and Technology of China, Chengdu, China.

His research interests include through-the-wall radar imaging and radio tomographic imaging.



**Guolong Cui** (Senior Member, IEEE) received the B.S. degree in electronic information engineering, and the M.S. and Ph.D. degrees in signal and information processing from the University of Electronic Science and Technology of China (UESTC), Chengdu, China, in 2005, 2008, and 2012, respectively.

From January 2011 to April 2011, he was a Visiting Researcher with the University of Naples Federico II, Naples, Italy. From June 2012 to August 2013, he was a Postdoctoral Researcher with the Department of Electrical and Computer Engineering, Stevens Institute of Technology, Hoboken, NJ, USA. From September 2013 to July 2018, he was an Associate Professor with UESTC, where since August 2018, he has been a Professor. His current research interests include cognitive radar, array signal processing, MIMO radar, and through-the-wall radar.



**Xiaqing Yang** (Student Member, IEEE) received the B.S. degree in electronic engineering in 2013 from the University of Electronic Science and Technology of China, Chengdu, China, where she is currently working toward the Ph.D. degree in signal and information processing.



**Shihao Fan** received the B.S. degree from the Hefei University of Technology, Hefei, China, in 2017. He is currently working toward the M.S. degree with the School of Information and Communication Engineering, University of Electronic Science and Technology of China, Chengdu, China.

His research interests include NLOS target detection in urban environment.



**Haining Yang** (Member, IEEE) received the B.S. degree in electronic engineering from Shandong Normal University, Jinan, China, in 2009, and the Ph.D. degree in signal and information processing from the University of Electronic Science and Technology of China (UESTC), Chengdu, China, in 2016.

From 2013 to 2015, he was a Visiting Researcher with the Department of Electrical Engineering, Duke University, Durham, NC, USA. From 2016 to 2017, he was a Research Assistant with the School of Electronic Engineering, UESTC. He is currently an Associate Researcher with the School of Electronic Science and Engineering, UESTC. His research interests include radar imaging, digital radar, and communication array.